Available online at www.sciencedirect.com
ScienceDirect
Journal of Power Sources 170 (2007) 345–358
JOURNAL OF POWER SOURCES
www.elsevier.com/locate/jpowsour

Mechanical behavior of fuel cell membranes under humidity cycles and effect of swelling anisotropy on the fatigue stresses

Ahmet Kusoglu [a], Anette M. Karlsson [a,*], Michael H. Santare [a], Simon Cleghorn [b], William B. Johnson [b]

[a] *Department of Mechanical Engineering, University of Delaware, Newark, DE 19716, United States*
[b] *Gore Fuel Cell Technologies, 201 Airport Road, P.O. Box 1488, Elkton, MD 21922-1488, United States*

Received 28 January 2007; received in revised form 16 March 2007; accepted 29 March 2007
Available online 12 April 2007

Abstract

The mechanical response of proton exchange membranes in a fuel cell assembly is investigated under humidity cycles at a constant temperature (85 °C). The behavior of the membrane under hydration–dehydration cycles is simulated by imposing a humidity gradient from the cathode to the anode. Linear elastic, plastic constitutive behavior with isotropic hardening and temperature and humidity dependent material properties are utilized in the simulations for the membrane. The evolution of the stresses and plastic deformation during the humidity cycles are determined using finite element analysis for two clamping methods and various levels of swelling anisotropy. The membrane response strongly depends on the swelling anisotropy where the stress amplitude decreases with increasing anisotropy. These results suggest that it may be possible to optimize a membrane with respect to swelling anisotropy to achieve better fatigue resistance, potentially enhancing the durability of fuel cell membranes.

Keywords: Proton exchange membrane (PEM); Nafion® membrane; Humidity cycle; Mechanical response; Elasto-plasticity; Swelling anisotropy

1. Introduction

Proton exchange membrane fuel cells (PEMFCs) are viable candidates for powering vehicles in a proposed future hydrogen economy. However, in order to replace the internal combustion engine, the durability and reliability of the fuel cell systems must be improved. For automotive applications the current target is 5000 h (150,000 miles equivalent) operational life over a full range of vehicle operating temperatures (−40 to 40 °C) [1].

During the operation of the cell, the proton exchange membrane (PEM) provides an ionic conductive path for protons from the anode to the cathode, while acting as an electronic insulator and a gas barrier to prevent mixing of oxygen and hydrogen. Any type of discontinuity in the membrane reduces the performance (i.e. output power, total voltage) and lifetime of the cell [2–6]. Although the electro-chemical and thermo-mechanical interactions among cell components (electrocatalysts, membranes, gas diffusion layers, and bipolar plates) affect the durability, it has been found that the membrane itself is a major source of failure, including mechanical damage and chemical degradation [2,3,5–8]. Thus, the membrane must be durable enough to withstand mechanical stresses and chemical attacks so that the fuel cell can sustain its function under the severe internal operating conditions.

Several forms of mechanical damage in the membrane electrode assembly (MEA) are commonly observed, including through-the-thickness tears or pinholes in the membrane, or delamination between the polymer membrane and the electrodes [4–10]. A number of studies related to the influence of the membranes' mechanical properties on the durability and performance of the cell are available in literature [2,3,9,11–13]. It is commonly believed that the mechanical stresses, due to the hydration–dehydration cycles in the membrane precipitate these damage mechanisms [9,14–16]. Kolde et al. [13] investigated the material properties and fuel cell performance of several commercial fuel cell membranes of various thicknesses. The results indicated that membranes exhibiting good dimensional stability in the in-plane directions during hydration–dehydration cycles are desirable for improving the cell performance and product reliability. A key parameter is therefore the swelling

* Corresponding author. Tel.: +1 302 831 6437; fax: +1 302 831 3619.
E-mail address: karlsson@udel.edu (A.M. Karlsson).

0378-7753/$ – see front matter © 2007 Elsevier B.V. All rights reserved.
doi:10.1016/j.jpowsour.2007.03.063

coefficient of the membrane [14,16,17]. Previous work simulating the mechanical response of a PEM during fuel cell operation [14] showed (through numerical means) that compressive stresses develop upon hygro-thermal loading. In some cases, these stresses can exceed the yield strength, causing permanent deformation. This, in turn, results in tensile residual stresses after dehydration. These in-plane tensile residual stresses are believed to be a significant contributor to the mechanical failures observed in the membranes, since they may cause the propagation of the through-the-thickness cracks in the membrane.

Even though crack initiation mechanisms in polymers are not completely understood, cyclic loading results in fatigue crack growth, which is one of the mechanisms governing the lifetime of these materials. The fatigue crack growth rate is governed by the stress amplitude and stress level [18,19]. Therefore, investigating the stresses in the membrane during hygro-thermal cycling, which is the objective of this paper, is an important part of understanding the failure mechanisms in the membrane.

A common method to experimentally simulate the fuel cell operation is with accelerated cycling through a range of inlet relative humidities (RH) at elevated temperatures (80–95 °C) [3,7,13,15,20,21]. Accelerated open-circuit voltage decay tests were conducted by Protsailo [20] using Nafion® membranes to identify the long-term effects of high temperature and low RH operation on the performance of the perfluorosulfonic acid (PFSA) membranes. They found that membrane lifetime increases with increased inlet humidity and decreases with an increase in operating temperature. In the case of reduced relative humidity, the membrane failure is accelerated by a degradation of the mechanical properties of the PFSA [20]. In order to demonstrate purely mechanical failure modes, several investigators conducted RH cyclic tests in the absence of electro-chemical reactions [7,15]. Mathias et al. [15] conducted an RH cycling test for an MEA made from a cast, 25 μm Nafion®[1] membrane. The MEA was held at a constant 80 °C and cycled between maximum and a minimum RH values in the absence of chemical degradation [15]. Recently, different test procedures were introduced to study the purely mechanical, and combined mechanical and chemical durability of fuel cell membranes for the development of new materials [7,21]. Crum and Liu [7] conducted accelerated and non-accelerated tests (representing realistic automotive duty cycles) for various GORE-SELECT®[2] membranes (produced by W.L. Gore & Associates Inc.). These tests were run at a constant temperature (80 °C) and varying inlet and outlet RH at the anode and cathode. In order to separate the effects of chemical degradation and mechanical fatigue, they performed the tests in an inert environment (nitrogen) to suppress chemical activity. Similar trends in the durability of membranes were observed for the both accelerated and non-accelerated tests [7]. Thus, accelerated RH cycling tests may be an effective way of simulating the automotive fuel cell duty cycles in order to observe the failure mechanisms and to monitor the durability and the changes in the material properties of the membrane [7,21].

In this work, we study the mechanical response of the membranes through numerical simulations. We employ a mechanics based model, that includes temperature and humidity dependent material properties, to determine the evolution of the stresses in the membrane due to the hydration–dehydration cycles at a fixed temperature (85 °C) corresponding to the maximum operating temperature of the fuel cell. The influence of the cell assembly design in terms of the clamping method is investigated (Fig. 1). In addition, since the swelling of the membrane induces the compressive stresses and subsequent residual tension, swelling anisotropy of the membrane will be investigated.

In the following, we review the theory for isotropic elasto-plasticity, followed by the definition of the geometry of the unit cell with boundary and loading conditions used in the numerical model. The material properties of the membrane used in this model are based on data obtained from our tensile tests of the membrane reported previously [17]. The details of the hygro-thermal loading cycles and the simulation of swelling strains during these cycles are studied. In Section 3, we introduce a series of assumed anisotropic swelling characteristics and evaluate their effects on the stresses.

2. Theory for isotropic elasto-plasticity

Here, we outline the approach used to incorporate hygro-thermal effects into the finite element simulation including isotropic plasticity. This is an extension of previous work, where first the linear-elastic [16], and later the linear-elastic, perfectly plastic behavior [14] of the membrane were considered. An uncoupled theory is assumed, for which the additional temperature changes brought about by the plastic strain are neglected.

We assume that the total strain tensor, ε_{ij}, can be written as the sum:

$$\varepsilon_{ij} = \varepsilon_{ij}^{\mathrm{e}} + \varepsilon_{ij}^{\mathrm{pl}} + \varepsilon_{ij}^{\mathrm{T}} + \varepsilon_{ij}^{\mathrm{S}}, \tag{1}$$

where $\varepsilon_{ij}^{\mathrm{e}}$ are the elastic strain components, $\varepsilon_{ij}^{\mathrm{pl}}$ are the plastic strain components, and $\varepsilon_{ij}^{\mathrm{T}}$ and $\varepsilon_{ij}^{\mathrm{S}}$ are the temperature and swelling induced strains, respectively. Assuming isotropic behavior, the thermal strains resulting from a change in temperature of an unconstrained isotropic medium are given by

$$\varepsilon_{ij}^{\mathrm{S}} = \alpha(T - T_0)\delta_{ij} \quad \text{with} \quad \delta_{ij} = \begin{cases} 1 & \text{if } i = j \\ 0 & \text{if } i \neq j \end{cases}, \tag{2}$$

where α is the linear coefficient of thermal expansion ($^\circ\mathrm{C}^{-1}$), T_0 and T are the reference and current temperature (°C), respectively, and δ_{ij} is the Kronecker delta.

Similarly, the swelling strains caused by moisture uptake are given by

$$\varepsilon_{ij}^{\mathrm{S}} = \varepsilon_{ij}^{\mathrm{S}}(T, H), \tag{3}$$

where T is the current temperature (°C) and H is the relative humidity (%). For an isotropic material, $\varepsilon_{ij}(T, H) = \varepsilon(T, H)\delta_{ij}$. In the current work, $\varepsilon^{\mathrm{S}}(T, H)$ is defined as a temperature and humidity dependent polynomial function based on the experimental data [17].

[1] Nafion is a registered trademark of E.I. DuPont De Nemours & Co.
[2] GORE-SELECT is a registered trademark of W.L. Gore & Associates Inc.

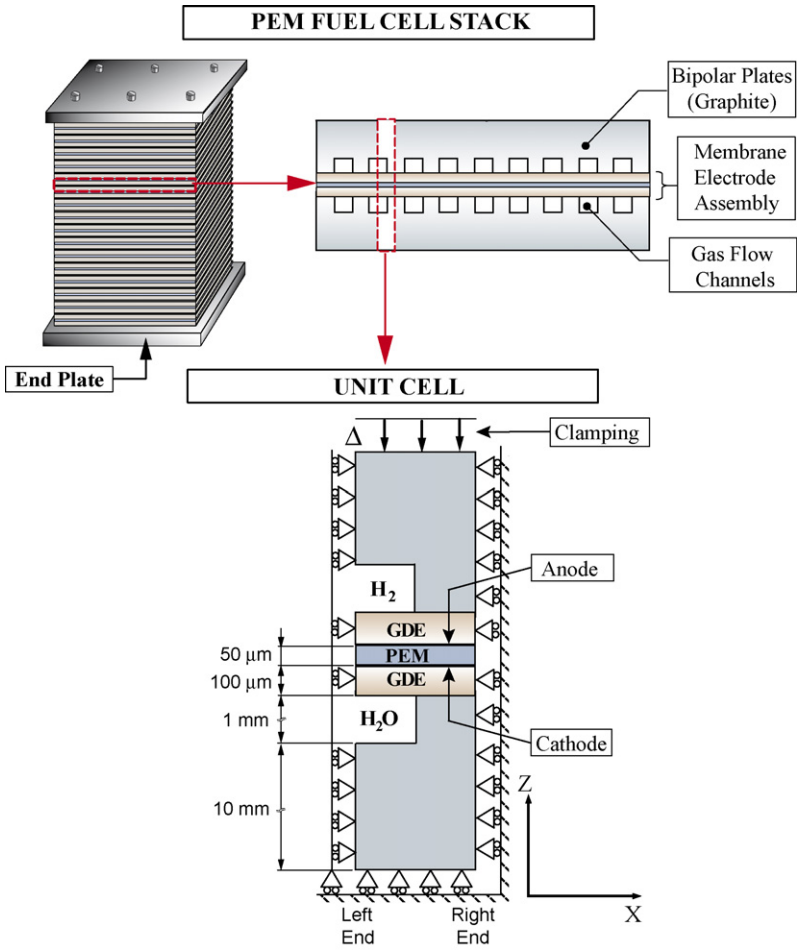

Fig. 1. The geometry of the unit cell used in the simulations. The mechanical boundary conditions are noted in the figure using symmetry assumptions. Two additional boundary conditions are imposed by subjecting the top of the stack to either constant displacement or constant force (not shown).

Assuming a linear response within the elastic region, isotropic Hooke's law is used to determine the stress tensor, σ_{ij}, and we have

$$\sigma_{ij} = \frac{E}{(1+\nu)(1-2\nu)}[\nu\delta_{ij}\varepsilon_{kk}^{\mathrm{el}} + (1-2\nu)\varepsilon_{ij}^{\mathrm{el}}], \tag{4}$$

where $\varepsilon_{kk} = \varepsilon_{xx} + \varepsilon_{yy} + \varepsilon_{zz}$, E is Young's modulus, and ν is Poisson's ratio. Based on our previously published experimental data [17], Young's modulus can be defined as a function of temperature and humidity, $E = E(T, H)$, and we assume Poisson's ratio remains constant. A generalized plane strain condition is imposed in the simulations:

$$\varepsilon_{xy} = \varepsilon_{yx} = \varepsilon_{yz} = \varepsilon_{zy} = 0 \quad \text{and} \quad \varepsilon_{yy} = \text{Constant}. \tag{5}$$

For the inelastic response, incompressible plastic deformation is assumed, with the rate-independent plastic flow according to the von Mises yield function (J_2-flow theory) [22]:

$$f(\sigma_{ij}) = \sqrt{\frac{3}{2}S_{ij}S_{ij}} - \sigma_0, \tag{6}$$

where σ_{ij} are the components of the (true) stress tensor, σ_0 the yield strength, and S_{ij} are the components of the deviatoric stress tensor defined by

$$S_{ij} = \sigma_{ij} - \frac{1}{3}\sigma_{kk}\delta_{ij}. \tag{7}$$

We further assume that the material exhibits isotropic hardening, thus the yield strength depends on the plastic strain as well as temperature and humidity, i.e.:

$$\sigma_0 = \sigma_0(\bar{\varepsilon}^{\mathrm{pl}}, T, H), \tag{8}$$

where $\bar{\varepsilon}^{\mathrm{pl}}$ is the current equivalent plastic strain:

$$\bar{\varepsilon}^{\mathrm{pl}} = \int \sqrt{\frac{2}{3}\,\mathrm{d}\varepsilon_{ij}^{\mathrm{pl}}\,\mathrm{d}\varepsilon_{ij}^{\mathrm{pl}}}. \tag{9}$$

In other words, this model considers isotropic expansion of the yield surface with plastic strain. According to the von Mises yield criterion, yield occurs when

$$f(\sigma_{ij}, \bar{\varepsilon}^{\mathrm{pl}}) = 0, \tag{10}$$

and the material deforms elastically for $f(\sigma_{ij}) < 0$. The Mises flow theory predicts that the plastic strain increment tensor is

proportional to the deviatoric stress tensor [22]:

$$d\varepsilon_{ij}^{pl} = d\bar{\varepsilon}^{pl} \frac{\partial f(\sigma_{ij}, \bar{\varepsilon}^{pl})}{\partial \sigma_{ij}} = d\bar{\varepsilon}^{pl} \frac{3}{2} \frac{S_{ij}}{\sigma_0}. \quad (11)$$

The equivalent plastic strain increment $d\bar{\varepsilon}^{pl}$ is determined from the condition that the yield criterion (Eq. (10)) must be satisfied during the strain hardening.

3. Numerical model

3.1. Assumptions

A previously developed two-dimensional finite element model [14,16] is adapted for the current simulations. The model includes the following simplifying assumptions:

(1) Simplified temperature profile with no heat generation.
(2) The electrodes are integrated into the gas diffusion layer (GDL) to form a GDE instead of considering them as a separate layer.
(3) For the GDE and the bipolar plate, the deformation is linear-elastic, with no swelling, while the membrane is allowed to deform plastically with isotropic hardening and swelling.
(4) All material properties are isotropic including the thermal expansions. However, isotropic and anisotropic swelling of the membrane is investigated.
(5) After the initial hygro-thermal loading to reach 85 °C, four humidity cycles are applied at this temperature, followed by hygro-thermal unloading.
(6) During humidity cycling, a linear humidity gradient through the membrane is imposed from cathode to anode, such that cathode humidity is cycled from 30% RH to 95% RH while the anode is kept at 30% RH.

3.2. Geometry and boundary conditions

The gas flow channels in the graphite plates are used to transport hydrogen to the anode side of the membrane electrode assembly (MEA) and air to the cathode, while the product water vapor is carried away. In previous studies [14,16], we selected two graphite plate alignments to study the effects of the geometry of the gas flow channels: (1) aligned and (2) alternating. We found that gas channel alignment primarily affects the *location* of the maximum stresses rather than the *magnitude*. Thus, for simplicity, in this study we will only investigate the aligned case in our simulations (see Fig. 1).

We used the commercial software ABAQUS 6.4 [23] with four-node, generalized plane strain temperature–displacement coupled elements (CPEG4T) for the simulations. For comparison purposes, eight-node elements with reduced integration (CPEG8RT) were also tried. Since no significant difference was found in the results, in the following, we will present the results from the four-node elements. A total of 21,200 elements were used in the model and 9×80 elements are used for the thickness and length of the membrane, respectively.

The thickness of the bipolar plates in the model is 11 mm, and the depth and the width of the gas channels in the plates are 1 mm each (Fig. 1). The membrane thickness is 50 μm (corresponding to the thickness of Nafion® 112 membrane at ambient conditions). As mentioned previously, the catalyst layer is included in the gas diffusion layer, forming a gas diffusion electrode (GDE) with a thickness of 100 μm.

Two different clamping methods are investigated: (1) fixed force, corresponding to the case where the fuel cell stack is equipped with springs to control the clamping force, and (2) fixed displacement where the graphite plates are clamped preventing any net deformation in the thickness direction. In the former case, a constant pressure (1 MPa) is applied on the surface of upper graphite plate. In the latter case, a fixed displacement is calculated by applying a 1 MPa load to an otherwise unloaded model, and the resulting displacement at the upper boundary is fixed throughout the analysis.

Referring to the unit cell in Fig. 1, symmetric boundary conditions, $u_z = 0$ at the bottom edge, and $u_x = 0$ on right edge of the unit cell are applied. In order to have uniform displacement at the left side of the membrane, a linear constraint $A_1 u_x^{N_1} + A_2 u_x^{N_2} = 0$ is applied on the left edge, where $A_1 = 1$ and $A_2 = -1$, N_1 is the node at the bottom left end and N_2 are the remaining nodes on the left side.

3.3. Material properties

Previous work has shown that the mechanical response of the membrane is highly nonlinear [14]. It is therefore important to implement, as much as possible, the true material properties. The material properties for the graphite plates are set to that of commercial graphite and for the carbon paper the properties are obtained from TORAY® TGP-H-030 [24]. It is assumed that these materials have linear thermo-elastic behavior and do not swell in the presence of moisture. The physical properties of the membrane and other components used in this study are shown in Table 1. Physical properties for the membrane were adopted from the DuPont™ Nafion® 112 (perfluorosulfonic acid) membranes data sheet [25] and listed in Table 1. For the mechanical properties of the membrane, we use the results of our experimental research, summarized in Tables 2 and 3 [17]. In the experimental study, tensile tests of the Nafion® 112 membrane films were conducted in an environmental chamber within a temperature range from 25 to 85 °C, and a relative humidity range from 30% RH to 90% RH to obtain true stress-true strain curves at each temperature–humidity point. The details of the experiments are discussed elsewhere [17]. Based on these results, linear-elastic, plastic behavior with isotropic hardening and temperature and humidity dependent material properties is used for the membrane. Young's modulus and the proportional limit (assumed to correspond to the yield strength) of the membrane are defined at four temperatures and four humidities. Even though a slight anisotropy in the material properties was observed experimentally [17], in this study we assume, for simplicity, that the material properties are isotropic.

The isotropic hardening used in the finite element program, ABAQUS [23], is defined by the initial yield strength,

Table 1
The physical properties of the materials used in the finite element analysis [24,25]

Units	k (W m K^{-1})	ρ (kg m^{-3})	E (MPa)	ν	α (10^{-6} K^{-1})	C_p (J kg K^{-1})
Bipolar plates (graphite)	95.0	1800	10,000	0.25	5.0	750
GDE (carbon paper)	0.3	400	10,000	0.25	−0.8	500
Membrane (Nafion® 112)	0.259	2000	Table 2	0.25	123.0	1050

Table 2
Young's modulus at various temperatures and humidities for Nafion® 112 membrane [17]

	Relative humidity (%)			
	30	50	70	90
Young's modulus[a] (MPa)				
T = 25 °C	197	192	132	121
T = 45 °C	161	137	103	70
T = 65 °C	148	117	92	63
T = 85 °C	121	85	59	46

[a] Linear interpolation between given data points is used during the loading and unloading.

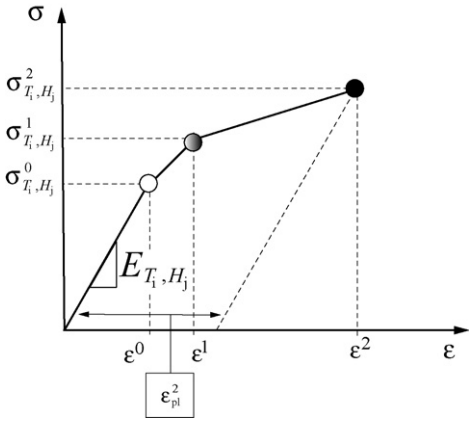

Fig. 2. Schematic representation of the temperature and humidity dependent stress–strain curves with hardening. The values of stresses at each combination of temperature and humidity (T_i, H_j) are given in Table 3(a–c) for the plastic strain values, ε^{pl} = 0, 0.05 and 0.25.

$\sigma^0(T, H; \varepsilon^{pl} = 0)$, where the plastic strain is assumed to be zero, and two additional stress points at $\sigma^1(T, H; \varepsilon^{pl} = 0.05)$, and $\sigma^2(T, H; \varepsilon^{pl} = 0.25)$. This is done for each temperature and humidity combination by using the available stress–strain curves of the material (Fig. 2).

To incorporate the experimental data for the swelling strain (Fig. 3) [17] into the FE model, a third degree polynomial is used for the measured swelling strains at four humidities (30–90%) for each temperature. This way, the swelling strain can be written as a polynomial function of humidity and temperature:

$$\varepsilon^S(T, H) = \sum_{i,j=1}^{4} C_{ij} T^{4-j} H^{4-i}, \quad (12)$$

where C_{ij} ($i, j = 1 \ldots 4$) are the constants of the polynomial and given in Table 4. A reference state of 30% RH is chosen, where the swelling strain is assumed zero for all temperatures (Fig. 3).

Table 3
The data points of the true stress–plastic strain curve of Nafion® 112 membrane given at various temperatures and humidities [17] for (a) yield strength, $\sigma^0(\varepsilon^{pl} = 0)$, (b) stresses at plastic strain 0.05, $\sigma^1(\varepsilon^{pl} = 0.05)$, and (c) stresses at plastic strain 0.25, $\sigma^2(\varepsilon^{pl} = 0.25)$

	Relative humidity (%)			
	30	50	70	90
Yield strength[a] (MPa)				
(a) $\varepsilon^{pl} = 0$				
T = 25 °C	6.76	6.51	5.66	4.20
T = 45 °C	5.67	5.21	5.01	3.32
T = 65 °C	5.14	4.58	4.16	2.98
T = 85 °C	3.61	3.44	3.08	2.20
(b) $\varepsilon^{pl} = 0.05$				
T = 25 °C	7.16	6.61	6.22	5.11
T = 45 °C	5.70	5.72	5.43	3.69
T = 65 °C	5.30	4.77	4.36	3.33
T = 85 °C	4.16	3.62	3.16	2.26
(c) $\varepsilon^{pl} = 0.25$				
T = 25 °C	9.71	9.26	8.65	8.88
T = 45 °C	7.31	7.34	7.48	6.18
T = 65 °C	6.55	5.92	5.73	5.78
T = 85 °C	5.04	4.28	4.22	4.31

[a] Linear interpolation between given data points is used during the loading and unloading.

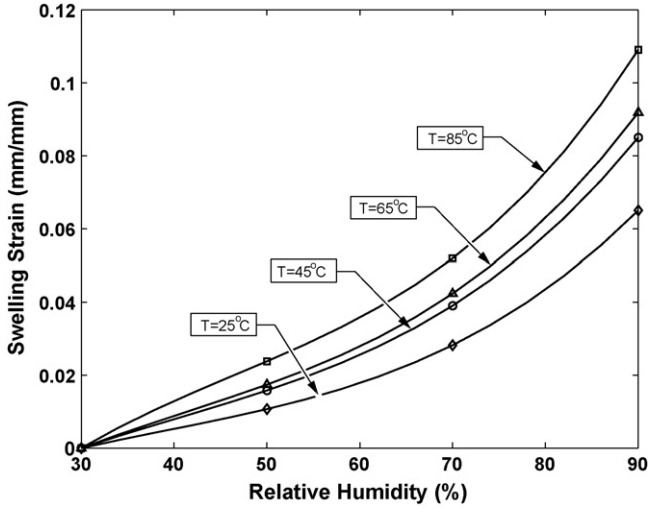

Fig. 3. Experimental data (markers) for the swelling expansion in the membrane and the polynomial curve fit (solid lines) to these data points as a function of humidity and temperature, plotted for four constant temperatures for Nafion® 112 [17].

Table 4
Constants for the swelling strain polynomial defined in Eq. (12)

	$i=1$	$i=2$	$i=3$	$i=4$
C_{ij}				
$j=1$	2.994×10^{-12}	-5.221×10^{-10}	3.574×10^{-8}	-6.832×10^{-7}
$j=2$	-4.303×10^{-10}	7.361×10^{-8}	-5.166×10^{-6}	1.003×10^{-4}
$j=3$	2.163×10^{-8}	-3.566×10^{-6}	2.564×10^{-4}	-5.067×10^{-3}
$j=4$	-5.402×10^{-8}	2.012×10^{-5}	-2.007×10^{-3}	4.355×10^{-2}

3.4. Simulation of hygro-thermal loading

We simulate a fuel cell duty cycle by first defining the "*initial conditions*," followed by conducting a loading sequence that can be summarized in four phases.

The initial conditions (corresponding to the assembly conditions) for the zero stress-state are defined as all components of the cell stack being set to room temperature 20 °C, and relative humidity 30%. Since we do not have experimental data for temperatures below 25 °C, the material properties below these values are assumed to be constant. The subsequent four load phases are:

- *Phase 1*. The *clamping condition* (fixed force or fixed displacement as described above) is applied as described in Section 3.2. This corresponds to assembling the stack.
- *Phase 2*. *Hygro-thermal loading* is applied by linearly increasing the relative humidity and temperature of the assembly simultaneously. A simplified temperature profile is imposed according to the assumption that the cathode/GDE and anode/GDE interface temperatures are at 85 and 86 °C, respectively (Fig. 4). The bipolar plate is assumed to have a constant temperature at its midplane, 80 °C, which is the cell operating temperature. These values correspond to a fuel cell operating at 80 °C under typical conditions based on results from [2]. The humidity is modeled either as a constant RH value through the membrane "*uniform loading*" or as a gradient through the thickness "*gradient loading*." In order to simulate the humidity gradient distribution in the membrane, a linear variation is imposed in the thickness direction of the membrane such that the anode remains at the initial humidity value (30% RH), while the maximum humidity (95% RH) is reached at the cathode side (Fig. 4). These parameters roughly model the real-life operating conditions of a humidified membrane [2]. We note that the PEM is assumed to be the only component to swell in the presence of humidity.
- *Phase 3*. *Hydration–dehydration cycle* is achieved by linearly decreasing and increasing the relative humidity between the initial (30% RH) and the hydrated (95% RH) conditions at the cathode, while the temperature is fixed at the maximum values (85/86 °C). This cycle is repeated four times (Fig. 5) (we will later see that a "cyclic steady state" is achieved, and further cycling will not provide additional information, within the context of this model).
- *Phase 4*. *Unloading* is achieved by linearly decreasing the relative humidity and temperature simultaneously, back to the initial values, but leaving the clamping conditions imposed.

The described sequence aims to simulate a typical accelerated test conducted to screen the performance and the durability of fuel cells [7,15]. This hygro-thermal loading cycle is a simplification of real-life operating condition that corresponds to taking the cell from start-up to a hydrated state and then back to the initial state. It is assumed that the cell remains at high tem-

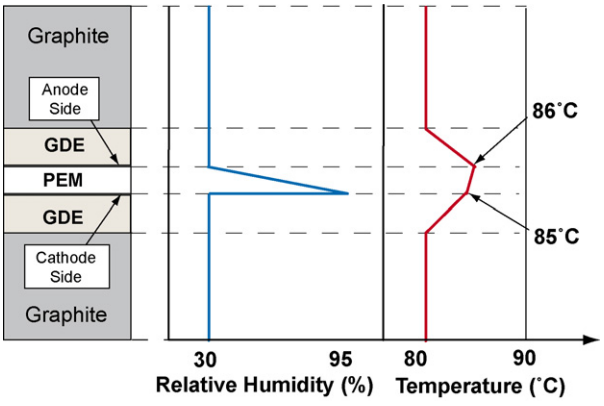

Fig. 4. The relative humidity and the temperature profiles in the membrane during the hydration–dehydration cycles at maximum thermal load. For the temperature profile of the unit cell, a constant anode/GDE temperature of 85 °C and cathode/GDE temperature of 86 °C is assumed [14,16], and a linear humidity gradient from cathode (fully humidified) through anode is imposed.

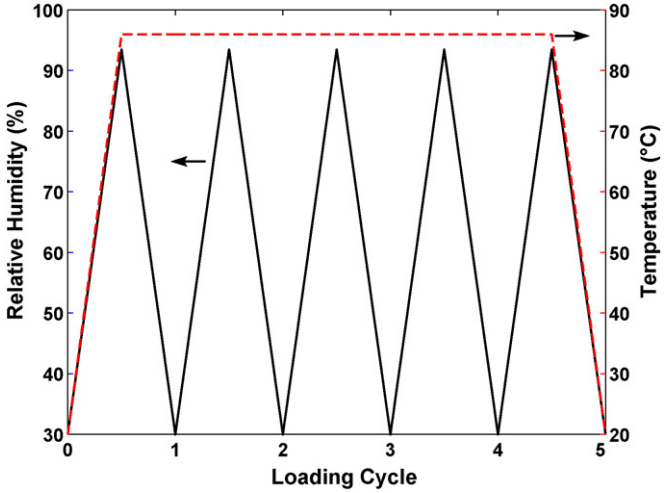

Fig. 5. The relative humidity and temperature cycle in the membrane used for the analysis. Since there is a gradient for both temperature and humidity as given in Fig. 4, given here are the maximum values the membrane reaches: maximum humidity (95% RH) at cathode side and maximum temperature (86 °C) at anode side.

perature during the rapid hydration–dehydration cycles, since cooling occurs at a much slower rate than drying in an operating fuel cell.

3.5. Simulating eigenstrain: swelling and thermal expansion

The strains in the membrane due to the humidity and temperature changes are calculated from the assumed thermal and swelling strains (Eqs. (2) and (3)), where the coefficient of thermal expansion is given in Table 1. The user subroutine UEXPAN [23] is used to define the strain increments during the hygro-thermal loading/unloading in the simulations.

3.5.1. Volumetric swelling strain

The volumetric swelling strain, ε_V, is defined as

$$\varepsilon_V = \frac{dV}{V_0} = (1+\varepsilon^S_{xx})(1+\varepsilon^S_{yy})(1+\varepsilon^S_{zz}) - 1, \quad (13)$$

where ε^s_{ii} are the components of the swelling strains in the normal directions ($i = x$, y or z) and dV and V_0 are the volume change and the initial volume, respectively.

Although swelling strains in the transverse and the machine direction exhibits a slight anisotropy [17], the swelling expansion behavior of Nafion® membrane is assumed isotropic [25]. At 85 °C and 95% RH the swelling strain in Nafion® 112 membrane is approximately 12% for both in-plane directions. Therefore, assuming isotropic material we have $\varepsilon_{xx} = \varepsilon_{yy} = \varepsilon_{zz} \cong 0.12$, where ε_{xx}, ε_{yy} are the in-plane (1, 2) and ε_{zz} is the out-of-plane (3) swelling strains. Finally, the volumetric strain according to Eq. (13) is

$$\varepsilon_V = \frac{dV}{V_0} = (1.12)^3 - 1 = 0.40. \quad (14)$$

In our simulations, we will first consider this assumed isotropic swelling followed by a study of anisotropic swelling effects on the mechanical response.

3.5.2. Modeling of isotropic swelling

When isotropic swelling is considered, the swelling strain is defined by a polynomial as a function of humidity and temperature, $\varepsilon^S(T, H)$ according to Eq. (12). The swelling strain increment, $\Delta\varepsilon^S(T, H)$, due to a temperature–humidity increment, is given by

$$(\Delta\varepsilon^S_{iso})_n = \varepsilon^S_{iso}(T_n, H_n) - \varepsilon^S_{iso}(T_{n-1}, H_{n-1}), \quad (15)$$

where n is the current loading increment and T_n (°C) and H_n (% RH) are the corresponding temperature and relative humidity values, respectively, at that increment. The subscript $n-1$ indicates the condition at the previous increment and the subscript "iso" indicates isotropic swelling strain. The total swelling strain during the hygro-thermal loading/unloading is then

$$\varepsilon^S_{iso}(T, H) = \sum_{n=1}^{N} (\Delta\varepsilon^S_{iso})_n, \quad (16)$$

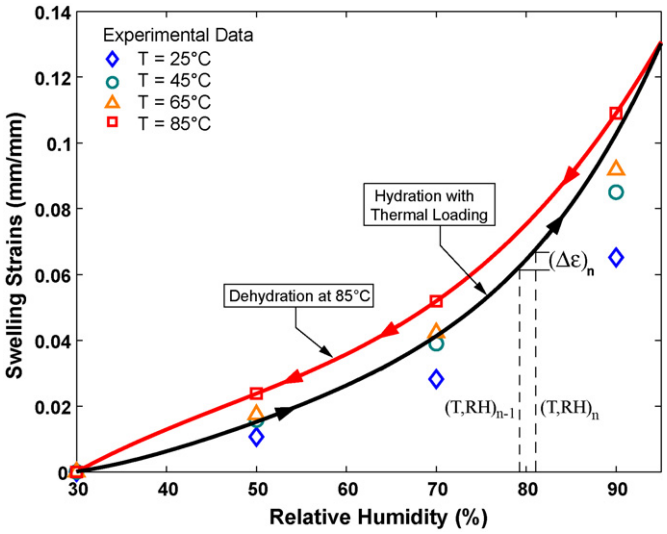

Fig. 6. The evolution of the swelling strains during the first hygro-thermal cycle, from (30% RH at 20 °C) to the hydrated state (95% RH at 85 °C), and during the humidity unloading from hydrated state to the dry state (30% RH at 85 °C) at constant temperature. The curves are plotted by using the swelling strain polynomial, $\varepsilon^S_{iso}(T, H)$, whose constants are obtained by an interpolation among the experimental data (markers) obtained at given a set of temperature and humidity.

where N is the total number of loading increments. The evolution of the swelling strain during the loading and unloading is shown in Fig. 6. Due to the nonlinear dependence on temperature and humidity, separate paths are taken during loading and unloading, but the initial and end points are same (by definition).

3.5.3. Modeling of anisotropic swelling

We make two assumptions for simulating anisotropic swelling expansion of the membrane:

(1) The total volume change of the fully hydrated anisotropic membrane due to the swelling is identical to the isotropic case (i.e. the maximum $\varepsilon^{aniso}_V = \varepsilon^{iso}_V = 0.40$). This corresponds to requiring the same total water uptake.
(2) The swelling expansions in the in-plane directions (x, y) are always equal ($\varepsilon^S_{xx} = \varepsilon^S_{yy} \neq \varepsilon^S_{zz}$).

Therefore, the anisotropy is introduced by increasing the swelling strain in the thickness direction (z), and calculating the corresponding swelling strains in the in-plane (x, y) directions using the constant volumetric swelling strain assumption. Three levels of anisotropy are investigated, ranging from the isotropic case to the "*fully anisotropic*" case (where the membrane swells only in the thickness direction). The swelling strain components calculated for each case are shown in Table 5.

To investigate the influence of swelling anisotropy, we modify the swelling strain increments for the isotropic case, by multiplying with the anisotropy ratio defined as

$$\text{Anisotropy ratio} = \frac{\text{Anisotropic swelling strain}}{\text{Isotropic swelling strain}} = \frac{\varepsilon^{S,i}_{aniso}}{\varepsilon^S_{iso}}, \quad (17)$$

Table 5
The values of the total swelling strains in the membrane in each direction for the isotropic and anisotropic cases used in the analysis (anisotropy ratios, $\varepsilon^{S,i}_{aniso}/\varepsilon^{S}_{iso}$ $(i = x, y)$ are given for each case, which are used to modify the subroutine)

	Isotropy	Anisotropy		
Swelling strains (mm mm^{-1}) at maximum humidity (95% RH) load				
Directions	12-12	15-10	27-5	40-0
In-plane: x	0.12	0.10	0.05	0
In-plane: y (=x)	0.12	0.10	0.05	0
Out-of-plane: z	0.12	0.157	0.27	0.40
$\varepsilon^{S,z}_{aniso}/\varepsilon^{S}_{iso}$	1	1.308	2.250	3.333
$\varepsilon^{S,x}_{aniso}/\varepsilon^{S}_{iso}$	1	0.833	0.416	0

where $\varepsilon^{S,i}_{aniso}$ represents the anisotropic swelling strain in i-direction. For example, the swelling strain increments for the "15-10" case (swelling strain of 0.157 in the thickness direction and 0.10 in the in-plane directions) is

$$\Delta\varepsilon^{15\text{-}10}_{zz} = \left(\frac{\varepsilon^{S,z}_{aniso}}{\varepsilon^{S}_{iso}}\right)\Delta\varepsilon_{iso} = \frac{0.157}{0.12}\Delta\varepsilon_{iso} = 1.308(\Delta\varepsilon_{iso}), \quad (18)$$

for thickness direction (z), and

$$\Delta\varepsilon^{15\text{-}10}_{xx} = \left(\frac{\varepsilon^{S,x}_{aniso}}{\varepsilon^{S}_{iso}}\right)\Delta\varepsilon_{iso} = \frac{0.10}{0.12}\Delta\varepsilon_{iso} = 0.833(\Delta\varepsilon_{iso}), \quad (19)$$

for in-plane directions (x, y), where ($\Delta\varepsilon^{iso}$) is given in Eq. (12). Other cases follow in a similar manner. The anisotropy ratios for the cases considered are given in Table 5. The thermal strains are assumed to be isotropic and the same for all cases.

The resulting thermal and swelling strains – calculated through the subroutine UEXPAN – at the cathode are depicted in Fig. 7, in both in-plane and thickness directions for the first cycle. The "12-12" case represents the isotropic swelling properties (Nafion® 112 membrane). The other curves represent the three levels of anisotropy considered. Since the cathode and anode sides of the membrane are subjected to different relative humidity values due to the assumed humidity gradient, the largest swelling strain occurs at the cathode side of the membrane, and there is no swelling at the anode side. We note that these strains drive the system.

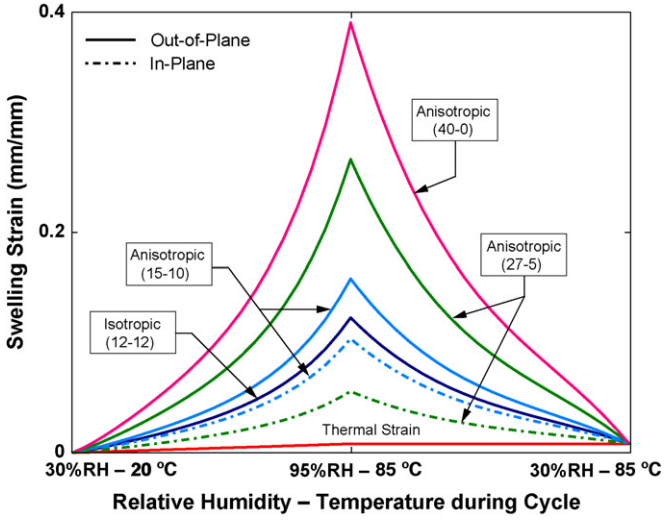

Fig. 7. The evolution of swelling strains during the first hygro-thermal cycle for the isotropic and three anisotropic cases, in the out-of-plane (thickness) (solid lines), and in-plane directions (dashed lines). The thermal strain is the same for all cases and plotted for comparison.

4. Results and discussion

4.1. Isotropic swelling

In a previous study [14] we found that, for the geometry considered, it is sufficient to focus on two locations in the membrane to study the maximum and minimum range and magnitude of the stresses: left end and right end, see Fig. 1. Therefore, the two end-points will primarily be used to investigate the evolution of the stresses and plastic deformation in the following. We note that the left end is the midpoint of the gas channel groove and the right end is the midpoint of the land (Fig. 1).

First, we investigate how the cyclic humidity loading affects the mechanical response of the membrane for two cases: (1) "uniform loading," using a uniform humidity distribution through the membrane during cycling, and (2) "gradient loading," using a humidity gradient from cathode to anode during cycling (Fig. 4). *Uniform loading* results in uniform in-plane stresses, whereas the *gradient loading* results in a stress gra-

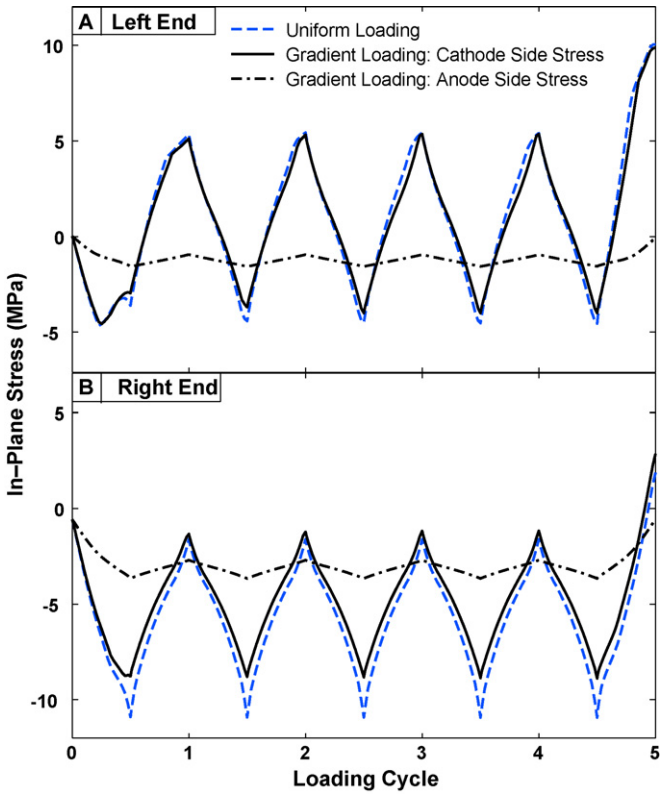

Fig. 8. Effect of the humidity loading conditions in the membrane on the evolution of in-plane stress at the "left end" (A) and the "right end" (B) of the membrane (Fig. 1). The results shown are for two cases: uniform humidity and linear humidity gradient in the membrane. In the latter case maximum humidity is imposed at the cathode side of the membrane.

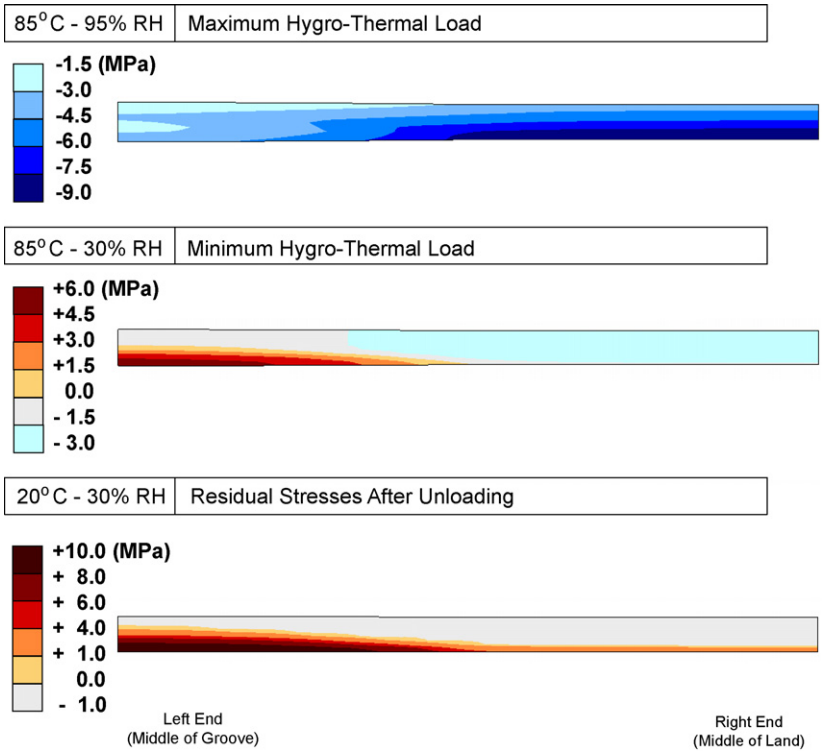

Fig. 9. Distribution of in-plane stresses in the membrane at maximum (95% RH at 85 °C) and minimum (30% RH at 85 °C) hygro-thermal load, and the residual stresses after unloading (30% RH at 20 °C) (for the fixed displacement case).

dient. Consequently, for the latter case, the in-plane stress is illustrated by showing the stresses at both the cathode and the anode side (Fig. 8). The gradient loading leads to similar stress levels at the cathode side of the membrane as those of the uniformly loaded case but the stress at the anode side remains low, due to the low humidity there. This results in a significant stress gradient associated with gradient loading. Such a stress gradient can become associated with bending of the membranes if delamination occurs between the PEM and the GDE, possibly accelerating the failure evolution of the membrane. In the remainder of this study, the gradient humidity loading will be considered.

The in-plane stress distribution in the membrane at maximum and minimum humidity loads and after unloading is depicted in Fig. 9 for gradient loading. The effect of the humidity gradient can be seen explicitly from these plots. The stresses at the cathode side of the membrane are larger than those of the anode side. Large compressive stresses are induced at maximum humidity load, and stresses are in tension at the minimum humidity load. After unloading, when both humidity and temperature decreases back to initial state, residual stresses up to 10 MPa are developed through the left of the membrane. Thus, the extreme maximum and minimum values of the stresses are localized at the left and right end of the membrane.

We showed in Fig. 7 that the contribution of the thermal strain is very small compared to the swelling strains. Thus, the in-plane stresses are mostly driven by the swelling strain. Furthermore, the inelastic strain (in this study the plastic (permanent) strain) is an important contributor to fatigue induced failures in cyclically loaded structures [18]. It is therefore of interest to study the individual strain components during the cyclic loading.

The contribution of each strain component in Eq. (1) (elastic, plastic, thermal and swelling) toward the total strain is plotted for the first cycle at the left and right ends of the membrane for the fixed displacement case (Fig. 10).[3] The initial hygro-thermal expansion is constrained by the surrounding structures (bipolar plates and GDEs), resulting in compressive elastic strains at both ends of the unit cell. The plastic strains remain zero until the yield limit is reached. When yielding starts, compressive in-plane plastic strains are induced due to the constraints at the ends. In the thickness direction, the resulting plastic strains are positive (due to incompressible deformation). Upon unloading, the elastic strains decrease, and go through a sign reversal eventually leading to reverse yielding.

The evolution of the magnitude of the equivalent plastic strain $\bar{\varepsilon}^{\mathrm{pl}} = \sqrt{(2/3)\varepsilon_{ij}^{\mathrm{pl}}\varepsilon_{ij}^{\mathrm{pl}}}$ at the cathode side shows that forward yielding (added plastic strain) and reverse yielding (subtracted plastic strain) are observed for each cycle (Fig. 11C). We also note that plastic strains are different at different locations in the membrane due to the different constraints (Figs. 10 and 11C).

The in-plane stress, σ_{xx}, and the out-of-plane stress, σ_{zz}, at the cathode side (Fig. 11A and B) both alternate between their respective upper and lower bounds, thus reaching a "cyclic steady state." These stress extrema are determined by the loading

[3] The elastic strains are not necessarily zero at the start of this cycle due to the initial clamping conditions imposed.

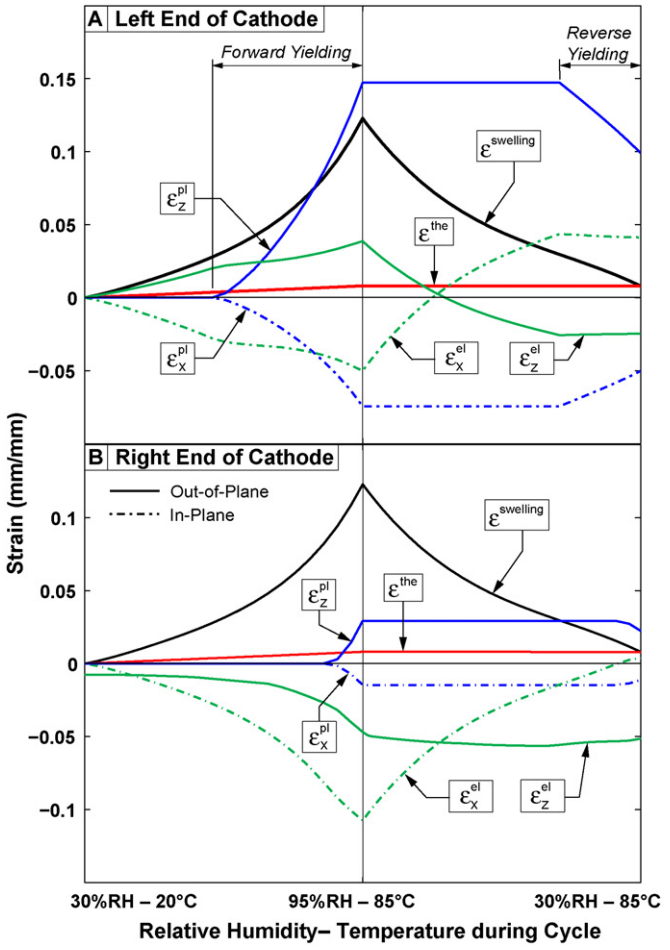

Fig. 10. (A and B) Contribution of thermal, swelling, plastic and elastic strains to the total strains in two directions; z (out-of-plane) and x (in-plane) for one humidity cycle, for the fixed displacement case. Due to the generalized plane strain assumption and the imposed boundary conditions, the strains in y-direction is equal to those of in x-direction.

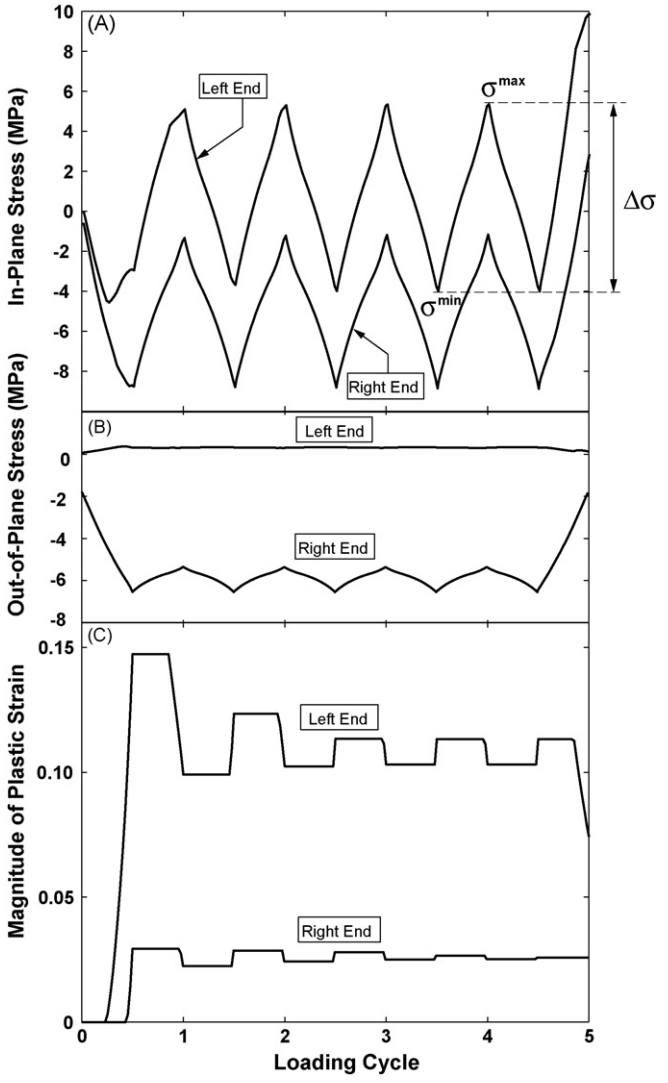

Fig. 11. Evolution of (A) in-plane, (B) out-of-plane stresses, and (C) the magnitude of equivalent plastic strain during the hygro-thermal cycles at three points of membrane's cathode side for the fixed displacement case and humidity gradient loading.

(temperature and humidity) and the yield strength of the membrane. Three important trends can be observed in Fig. 11A and B: (i) the magnitude of the out-of-plane stress is always smaller than the in-plane stress, (ii) at the left end, the in-plane stresses cycle between tensile and compressive loads, whereas the out-of-plane stresses cycle between two compressive values, and (iii) at the right end, all stress components cycle between two compressive values. Repeated fluctuation between tensile and compressive stresses, accompanied by cyclic yielding, is a more severe load case for fatigue compared to cyclic compressive stresses, and may be the cause of mechanical failure. We note that at the right end (midpoint of the land), the in-plane stresses remain compressive during cycling. Alternating between two compressive stress levels tends to be less likely to cause mechanical fatigue failure.

4.2. Anisotropic swelling

In this section, the effects of anisotropic swelling strain are investigated. The three anisotropic cases considered are designated; "10-15", "27-5" and "40-0" (fully anisotropic) (see Section 3.5.3 for definitions and Table 5 for values). With the in-plane stress exhibiting the largest (cyclic) tensile stresses, as discussed above, we will limit the following discussion to the in-plane stress component, for brevity.

The evolution of the in-plane stress at the two ends of the membrane is shown in Fig. 12 and corresponding plastic strain in Fig. 13 for the cases of anisotropic swelling considered. As can be seen from Fig. 12, increasing anisotropy leads to lower stresses at both ends. For the fully anisotropic case (40-0), the left end remains elastic during the cycling (Fig. 13A). For this case, the major contribution to the stresses comes from the clamping forces. For all cases with anisotropy, the right end experiences compressive stress (Fig. 12B) and yields only during the initial and final step (Fig. 13B) as opposed to the isotropic case, which exhibits cyclic yielding.

The magnitude of the equivalent plastic strain at the left end of the model (the midpoint of the groove) is larger than at the right end (the midpoint of the land), and decreases with increasing

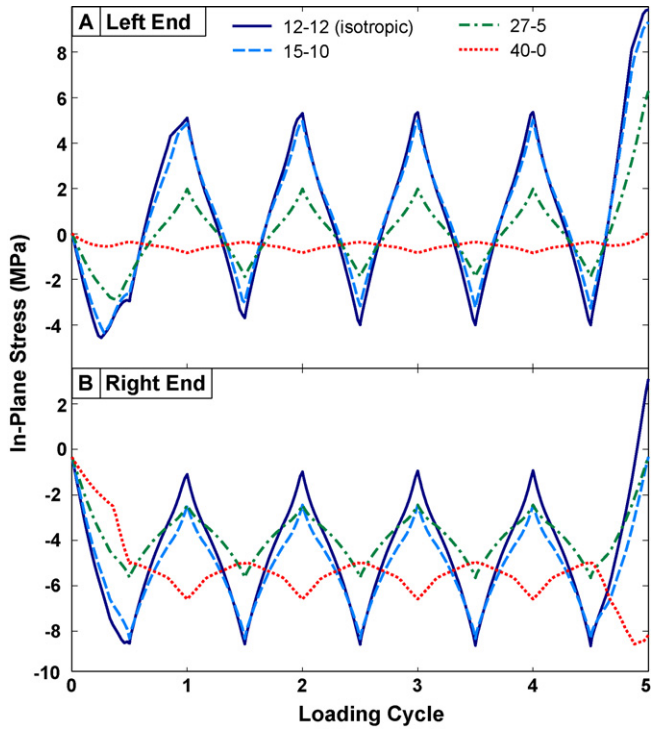

Fig. 12. The evolution of in-plane stresses for the fixed displacement case at (A) the left end and (B) the right end of the cathode side of the membrane plotted for different anisotropies.

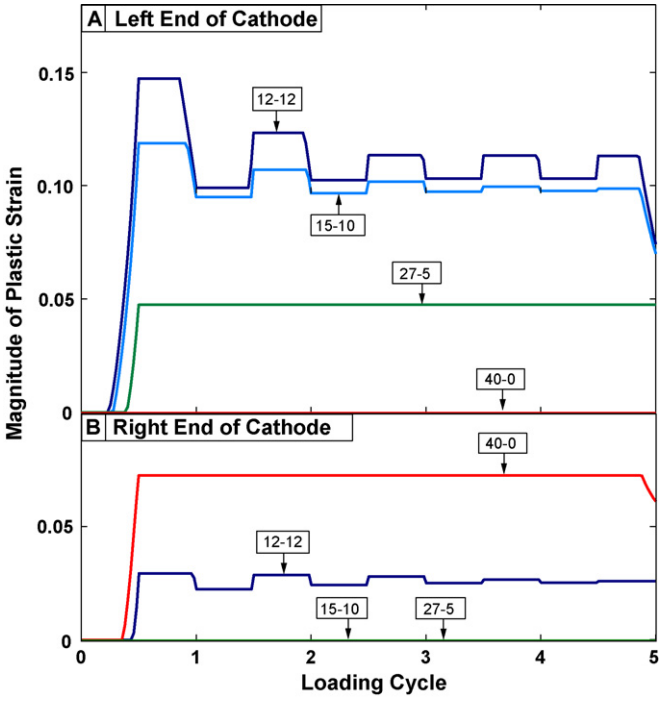

Fig. 13. The evolution of equivalent plastic strain magnitude for the fixed displacement case at (A) the left end and (B) the right end of the cathode side of the membrane, plotted for different anisotropies (constant plastic strain corresponds to elastic response).

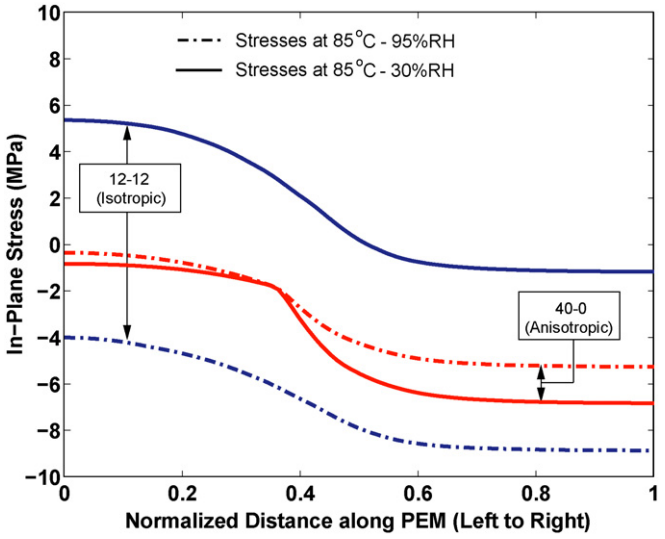

Fig. 14. The in-plane stresses, obtained after hydration and dehydration, respectively, during one hydration cycle plotted as a function of distance along the membrane for isotropic and anisotropic cases for fixed displacement. The arrows indicate the stress amplitude, the difference between the maximum and minimum stress, the membrane reaches during the cycle.

anisotropy (Fig. 13). The membrane swells more in the in-plane direction with decreasing anisotropy and therefore the equivalent plastic strain magnitude at the left end increases. Constraints at the right end of the membrane prevent the expansion in all directions leading to a hydrostatic state of stress, which inhibits yielding according to the Mises yield criteria (Eqs. (6)–(10)).

For the fully anisotropic case (40-0), the lack of swelling in the in-plane direction reduces the overall magnitude of stress resulting in vanishing plastic strain at the left end. No plastic strain develops at the left end. However, at the right end, large swelling of the membrane in the thickness direction leads to plastic deformation in the absence of hydrostatic stress.

The in-plane stress distributions along the membrane at maximum humidity load (95% RH) and after unloading (30% RH) are plotted for one cycle (the fourth cycle) in Fig. 14. In addition, the residual in-plane stresses at the cathode after cycling (end of the cyclic loading, 30% RH—20 °C) are plotted (for all cases) as a function of distance along the membrane, in Fig. 15. From Figs. 14 and 15 we see that the tensile stresses are highest at the left end of the model. This is due to the large plastic deformation occurring at these locations (Fig. 13A). At the right end (midpoint of the land), the smaller amount of yielding results in smaller residual stresses. For the fully anisotropic case, as discussed previously, there is no residual in-plane tensile stress for the left side of the model and most of the stresses come from the clamping load. However, for the right side, constraints prevent the thickening of the membrane, causing large compressive in-plane stresses.

4.3. Effect of membrane thickness

In order to examine the influence of the membrane thickness on the in-plane stresses, hypothetical membranes of thickness 20 μm (with the same material properties as used above), are

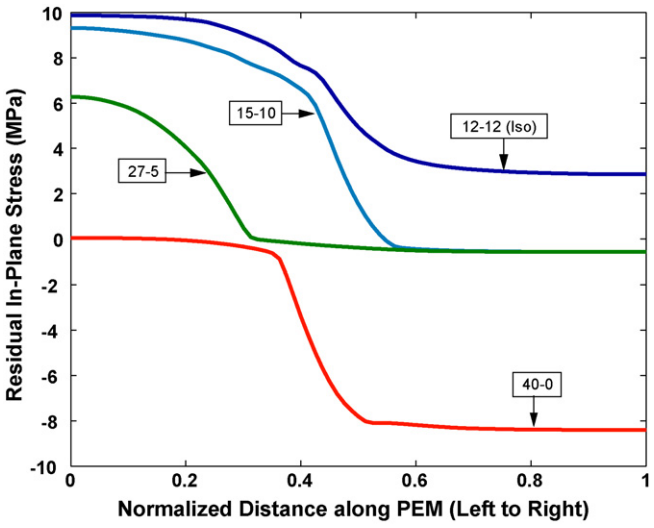

Fig. 15. The distribution of residual in-plane stress along the membrane obtained at the end of the five cycles (after hygro-thermal unloading from hydrated state to the initial state; 30% RH—20 °C) for the isotropic and anisotropic cases, and fixed displacement.

studied for the cases of isotropic (12-12) and fully anisotropic (40-0) swelling. In the previous subsections we have shown that the left and right ends of the model (midpoints of the groove and land) have the highest magnitudes of stresses during cycling (also see [14]). Thus, these stress amplitudes will be used to investigate the effect of membrane thickness. The in-plane stress amplitudes and the maximum stresses at the left and right ends of this hypothetical membrane (thickness: 20 μm) are given in Fig. 16A and B for the two cases studied, compared with the original membrane of thickness 50 μm.

For isotropic swelling, in-plane stress amplitudes, $\Delta\sigma = \sigma_{\max}^{\mathrm{RH=30\%}} - \sigma_{\min}^{\mathrm{RH=95\%}}$, (Fig. 16A) and maximum in-plane stress, $\sigma_{\max}^{\mathrm{RH=30\%}}$, (Fig. 16B) both decrease for the thinner membrane, especially at the left end of the membrane. For fully anisotropic swelling, the thickness has little effect on the in-plane stresses. This stress reduction may seem counter intuitive (i.e. it seems a thinner membrane should give larger stresses), however since this is a *strain-controlled* problem, the thickness of the membrane plays a secondary role when determining the stresses. In summary, even though the membrane thickness affects the stresses, the change in swelling of the membrane is a more important factor governing the stresses.

4.4. Effect of clamping conditions

So far, the effects of anisotropy and thickness on the stresses and plastic deformation in the membrane have been examined for the fixed displacement clamping condition. As in the previous subsection, stress amplitudes will be used to investigate the effect of the clamping conditions (fixed displacement and fixed force). Accordingly, the values of the stress amplitude, $\Delta\sigma = \sigma_{\max}^{\mathrm{RH=30\%}} - \sigma_{\min}^{\mathrm{RH=95\%}}$, and the maximum stress, $\sigma_{\max}^{\mathrm{RH=30\%}}$, in the in-plane direction, for the left and right ends of the membrane, for both clamping methods are shown in Fig. 17 during the fourth cycle, for the isotropic and the anisotropic cases.

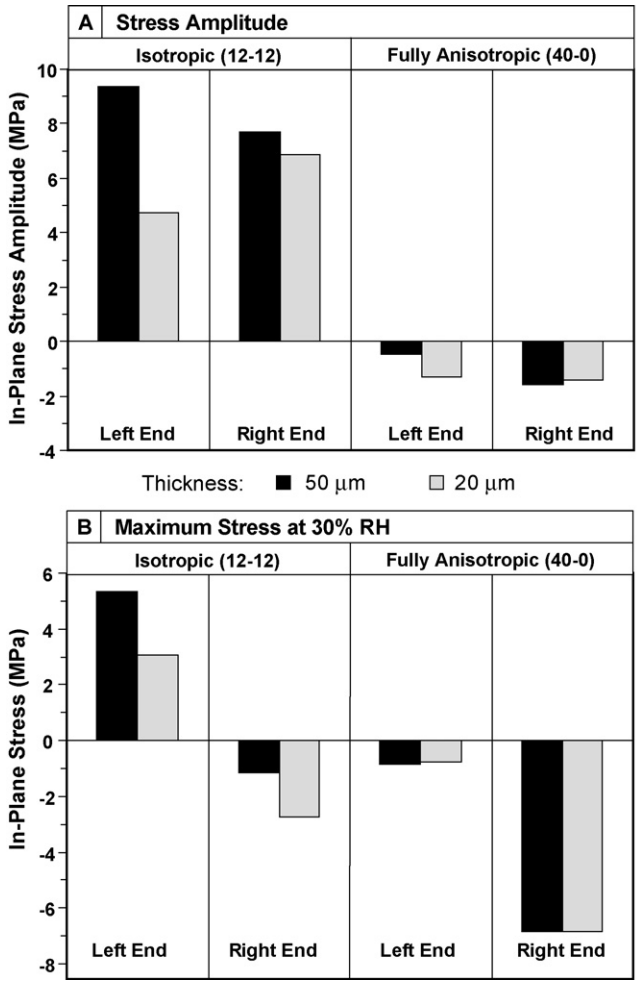

Fig. 16. (A) The in-plane stress amplitude ($\Delta\sigma_{xx} = \sigma_{xx}^{\mathrm{RH=30\%}} - \sigma_{xx}^{\mathrm{RH=95\%}}$) and (B) the maximum in-plane stress ($\sigma_{xx}^{\mathrm{RH=30\%}}$), at the left and right end of the membrane during the fourth cycle, for two thicknesses: 50 μm and 20 μm, for isotropic and fully anisotropic cases, and for fixed displacement case.

The stress amplitude decreases significantly with increasing anisotropy (Fig. 17A) since the membrane swells less in the in-plane direction. Moreover, the in-plane stresses at the minimum humidity load, 30% RH (Fig. 17B), tend to decrease with increasing anisotropy. All maximum stresses are tensile except for the fully anisotropic case and for the right end of the fixed displacement case, where the maximum in-plane stress is compressive due to the absence of reverse yielding (Figs. 12 and 13). Therefore, this may be interpreted as an advantage of the fully anisotropic swelling since compressive stresses reduce the risk of propagating any existing flaws in the membrane.

In previous studies, we investigated a case where the gas channels are not aligned. In general, the maximum stresses are similar to those of the aligned case and not shown here for brevity. However, in the alternating case, the large compressive stresses are in the midpoint of the model, instead of the right end [14].

In conclusion, increasing anisotropy results in a significant decrease in the stress amplitudes in the in-plane direction. Thus, it appears that increasing swelling anisotropy may be associated with reduced fatigue loading.

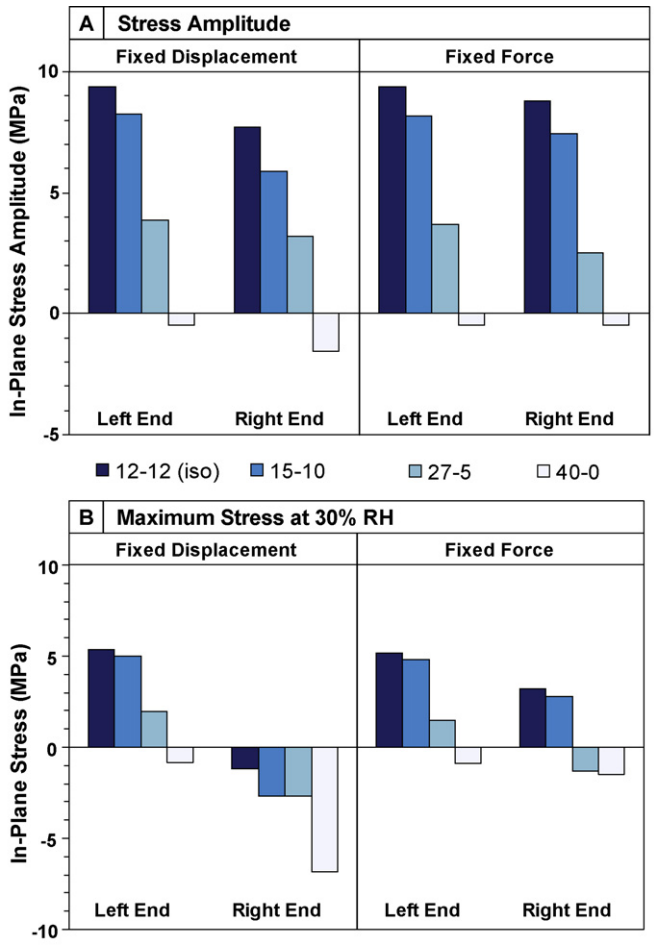

Fig. 17. (A) The in-plane stress amplitude ($\Delta\sigma_{xx} = \sigma_{xx}^{RH=30\%} - \sigma_{xx}^{RH=95\%}$), and (B) the maximum in-plane stress ($\sigma_{xx}^{RH=30\%}$), at the left and right end of the membrane during the fourth cycle, for isotropic and anisotropic cases, and for fixed displacement and fixed force cases.

5. Concluding remarks

Hydration–dehydration cycles at constant temperature (∼85 °C) are simulated in this numerical investigation to study the mechanical response of fuel cell proton exchange membranes, utilizing a unit cell approach. Both the case of uniform humidity loading and gradient humidity loading are considered. When a humidity gradient over the membrane is assumed, the cathode is subjected to cyclic humidification but the anode remains at ambient humidity during the cycling, with the intention of simulating conditions in an accelerated relative humidity (RH) cycling test. The mechanical model of the membrane assumes linear-elasticity with isotropic-hardening plasticity, and temperature–humidity dependent material properties based on our experimental studies of Nafion® membranes.

Uniform humidity loading conditions result in a uniform stress distribution over the thickness of the membrane. Large in-plane tensile stresses are observed in the middle of the groove ("left end" of the model). For the case of a humidity gradient through the membrane thickness, a stress gradient is generated, leading to large stress amplitudes (where the stress amplitude denotes the difference between the maximum and minimum stress during one full cycle). Thus, within the framework of this study, mechanical failure is most likely to occur at the cathode side of the membrane. However, experimental evidence is needed to confirm these results.

The results show that the in-plane swelling of the membrane due to water absorption is the primary driving force of the system for these types of load conditions, mainly causing large in-plane stresses. Our results show that swelling has a more profound effect on the stresses than either the clamping conditions or the membrane thickness.

The influence of swelling anisotropy is also studied. To this end, a constant volume change due to swelling was assumed, where the decreased swelling strains in the in-plane directions correspond to an increased swelling in the thickness direction. As expected, the in-plane stress amplitudes decrease with decreasing in-plane swelling, referred to as increasing swelling anisotropy. Since the in-plane stress is the major stress component in the membrane, and may cause the propagation of the minor flaws during cyclic loading, the parameters that affect the in-plane stress may have a direct influence on the fatigue behavior of the membrane. Furthermore, for fully anisotropic swelling, the membrane does not swell in the in-plane directions and the stresses never become tensile but remain compressive, a favorable outcome for the durability of the membrane. These findings suggest that membranes with low in-plane swelling strains during hydration–dehydration cycles may exhibit better performance during cell operation, which corresponds to the experimental results presented by Kolde et al. [13].

In conclusion, by designing the swelling anisotropy of the membrane, reduced stresses and therefore better fatigue resistance for PEM may be obtained that will ultimately improve the durability of the fuel cell.

Acknowledgements

This research has been supported by W.L. Gore & Associates Inc. and the State of Delaware Development Office (DEDO).

References

[1] DOE (Department of Energy)—MultiYear Research, Development and Demonstration Plan Planned Activities for 2003–2010 (Draft 6/3/03), vol. 3.4.4, 2003.
[2] U. Beuscher, S.J.C. Cleghorn, W.B. Johnson, Int. J. Energy Res. 29 (2005) 1103–1112.
[3] S. Cleghorn, J. Kolde, W. Liu, in: V. Wolf, L. Arnold, G. Hubert (Eds.), Handbook of Fuel Cells—Fundamentals, Technology and Applications, John Wiley & Sons Ltd., 2003.
[4] W. Liu, K. Ruth, G. Rusch, J. New Mater. Electrochem. Syst. 4 (2001) 227–232.
[5] J. Xie, D.L. Wood III, D.M. Wayne, T.A. Zawodzinski, P. Atanassov, R.L. Borup, J. Electrochem. Soc. 152 (2005) 104–113.
[6] S. Kundu, M.W. Fowler, L.C. Simon, S. Grot, J. Power Sources 157 (2006) 650–656.
[7] M. Crum, W. Liu, Effective Testing Matrix for Studying Membrane Durability in PEM Fuel Cells. Part 2. Mechanical Durability and Combined Mechanical and Chemical Durability, vol. 3. Electrochemical Society Inc., Pennington, NJ 08534-2896, United States, Cancun, Mexico, 2006, pp. 541–550.

[8] D.A. Dillard, M. Budinski, Y.-H. Lai, C. Gittleman, Proceedings of the 3rd International Conference on Fuel Cell Science, Engineering, and Technology, Ypsilanti, MI, United States, 2005, pp. 153–159.
[9] Y.-H. Lai, C.S. Gittleman, C.K. Mittelsteadt, D.A. Dillard, Proceedings of the 3rd International Conference on Fuel Cell Science, Engineering, and Technology, Ypsilanti, MI, United States, 2005, pp. 161–167.
[10] V. Stanic, M. Hoberecht, Mechanism of Pin-Hole Formation in Membrane Electrode Assemblies for PEM Fuel Cells, Electrochemical Society Inc., Pennington, NJ 08534-2896, United States, Honolulu, HI, United States, 2004, p. 1891.
[11] D.E. Curtin, R.D. Lousenberg, T.J. Henry, P.C. Tangeman, M.E. Tisack, J. Power Sources 131 (2004) 41–48.
[12] R.C. McDonald, C.K. Mittelsteadt, E.L. Thompson, Fuel Cells 4 (2004) 208–213.
[13] J.A. Kolde, B. Bahar, M.S. Wilson, T.A. Zawodzinski, S. Gottesfeld, Proceedings of the First International Symposium on Proton Conducting Membrane Fuel Cells, vol. 95-23, The Electrochemical Society Inc., 10 South Main Street, Pennington, NJ 08534-2896, 1995, pp. 193–201.
[14] A. Kusoglu, A.M. Karlsson, M.H. Santare, S. Cleghorn, W.B. Johnson, J. Power Sources 161 (2006) 987–996.
[15] M.F. Mathias, R. Makharia, H.A. Gasteiger, J.J. Conley, T.J. Fuller, C.J. Gittleman, S.S. Kocha, D.P. Miller, C.K. Mittelsteadt, T. Xie, S.G. Van, P.T. Yu, Electrochem. Soc. Interf. 14 (2005) 24–35.
[16] Y. Tang, M.H. Santare, A.M. Karlsson, S. Cleghorn, W.B. Johnson, J. Fuel Cell Sci. Technol. 3 (2006) 119–124.
[17] Y. Tang, A.M. Karlsson, M.H. Santare, M. Gilbert, S. Cleghorn, W.B. Johnson, Mater. Sci. Eng. A 425 (2006) 297–304.
[18] S. Suresh, Fatigue of Materials, Cambridge University Press, New York, 1991.
[19] K. Sadananda, A.K. Vasudevan, Mater. Sci. Eng. A 387–389 (2004) 536–541.
[20] L. Protsailo, DOE Hydrogen Program Review, Arlington, VA, 2006.
[21] S. Cleghorn, J. Kolde, Proceedings of Fuel Cell Seminar, Palm Spring, CA, 2005, p. 138.
[22] R. Hill, The mathematical Theory of Plasticity, Clarendon Press, Oxford, 1950.
[23] ABAQUS, ABAQUS Analysis User's Manual, HKS Inc., 2003.
[24] Toray Product Information, Toray Industries Inc.
[25] DuPont, Product Information: Nafion PFSA Membranes N-112, NE-1135, N-115, N-117, NE-1110 Perfluorosulfonic Acid Polymer, NAE101, 2004.